Chemical Science

ROYAL SOCIETY OF CHEMISTRY

EDGE ARTICLE

View Article Online
View Journal | View Issue

Cite this: *Chem. Sci.*, 2025, **16**, 15417

All publication charges for this article have been paid for by the Royal Society of Chemistry

Dipole induction by structural engineering of supports for Fe single-atom photocatalysts toward excellent photocatalytic ozonation†

Jing Wang,[ab] Haoxin Mai,[c] Jiakai Qiu,[a] Yanjun Xu,[d] Zhuan Wang,[d] Shenning Liu,[e] Yuxian Wang,[e] Yongbing Xie,*[ab] Rachel A. Caruso[c] and Hongbin Cao[ab]

Efforts in designing efficient polymer-based single atom photocatalysts (SAPs) have primarily focused on selecting specific metal atoms with tailored geometries and properties to control functionality. However, the impact of the light-harvesting units that bridge these single metal atoms, crucial for light absorption and energy transfer, has been largely overlooked. In this work, two carbon nitride (CN)-based iron SAPs with a similar FeN_4 coordination environment are synthesized: triazine-based CN (C_3N_4) and nitrogen-rich triazole-based CN (C_3N_5), differing in the unit cell structure. C_3N_5 exhibits better photocatalytic ozonation performance than C_3N_4 due to its unit cell asymmetry, which induces a dipole field that facilitates charge transfer. The addition of iron single atoms breaks the symmetry of C_3N_4 to enhance the dipole moment, while they weaken the separation and migration of bulk charge carriers in the Fe-C_3N_5 SAP. The iron atoms act as active sites in both Fe-C_3N_4 and Fe-C_3N_5 SAPs, accelerating interfacial reaction kinetics. These findings demonstrate the importance of the light-harvesting unit structures of CN-based SAPs in regulating photogenerated charge kinetics and offering valuable insights for the rational design of effective photocatalysts.

Received 24th March 2025
Accepted 19th July 2025

DOI: 10.1039/d5sc02256h

rsc.li/chemical-science

Introduction

Polymer-based semiconductors, with abundant anchoring sites and visible light responsiveness, are promising supports for single-atom photocatalysts (SAPs) in environmental pollution mitigation through reactive oxygen species (ROS) production.[1–3] Traditionally, enhancing SAP functionality and structural diversity has focused on manipulation of the metal atom and its coordination environment, that is, the type of metal and the atoms it coordinates with, to establish clear structure–activity relationships.[4–8] However, the influence of the unit cell structure of the support, where the metal anchoring sites reside, has received less attention despite its critical role in SAP design and performance. While single atoms (SAs) can induce charge transfer states between metal centers and ligands within the forbidden band of the photocatalyst material, thus broadening light absorption to longer wavelengths, the properties of the polymer-based support fundamentally dictate the light-harvesting capacity.[9–11] In addition, the SAs boost the separation and transfer of photogenerated charges by acting as charge pumps or introducing trap states, which facilitate the accumulation of surface charges and thus accelerate the target reactions.[12] Nevertheless, the specific role of SAs in the charge dynamics may vary depending on the structural unit of the support, leading to distinct photocatalytic behavior. Subtle variations in the structural unit of the support can also influence the metal–support interaction, altering surface reaction kinetics. Despite the profound impact of polymer support structures on photocatalytic mechanisms, a systematic study into how unit cell variations affect SAP performance remains underexplored.

Carbon nitrides (CNs) are promising polymer-based semiconductors with versatile structural tunability, rendering them ideal for a range of applications, such as photocatalytic hydrogen evolution and photocatalytic H_2O_2 generation.[13–15] Among CN materials, C_3N_4 with a tri-*s*-triazine symmetry unit structure has been widely used as a support for SAPs, as the nitrogen atoms within the framework provide abundant anchoring sites for single metal atoms.[16] In contrast, nitrogen-rich triazole-based carbon nitride (C_3N_5) with a lower C/N ratio exhibits an asymmetrical structure resulting from the polymerization of triazole and triazine frameworks, which can lead

[a]*Chemistry & Chemical Engineering Data Center, Institute of Process Engineering, Chinese Academy of Sciences, Beijing 100190, China. E-mail: ybxie@ipe.ac.cn*

[b]*School of Chemical Engineering, University of Chinese Academy of Sciences, Beijing 100049, China*

[c]*Applied Chemistry and Environmental Science, School of Science, STEM College, RMIT University, Melbourne, Victoria 3000, Australia*

[d]*Beijing National Laboratory for Condensed Matter Physics, CAS Laboratory of Soft Matter Physics, Institute of Physics, Chinese Academy of Sciences, Beijing 100190, China*

[e]*State Key Laboratory of Heavy Oil Processing, State Key Laboratory of Petroleum Pollution Control, China University of Petroleum-Beijing, Beijing 102249, China*

† Electronic supplementary information (ESI) available. See DOI: https://doi.org/10.1039/d5sc02256h

to distinct carrier behaviors compared to C_3N_4.[17] For example, recent studies have demonstrated that C_3N_5 with its asymmetrical structure overcomes the random distribution state of photogenerated carriers by inducing self-polarization to facilitate rapid, directional electron transfer, which is absent in C_3N_4.[18] Moreover, both C_3N_4 and C_3N_5 possess similar rich N sites, allowing for comparable single-atom coordination environments.[19] Therefore, comparing C_3N_4 and C_3N_5 as supports in SAPs provides a valuable platform to elucidate how the incorporation of symmetric triazine *versus* asymmetric triazole units in CN materials influences their charge transfer dynamics and photocatalytic activity, which is crucial for advancing CN-based photocatalysts in environmental remediation and other photocatalytic applications.

To promote the effectiveness of photocatalytic applications in environmental remediation, facilitating the formation of photo-induced radicals, particularly hydroxyl radicals ($^{\bullet}OH$, $E_0 = 2.80$ V_{NHE}), is paramount.[20] Strategies for producing $^{\bullet}OH$ *via* the reaction between electrons or holes and various acceptors in photocatalysis, such as O_2, O_3, H_2O, and H_2O_2 oxidants, have been developed.[21–23] Among these, photocatalytic ozonation stands out due to its high efficiency and selectivity by utilizing the oxidant (O_3) and photogenerated electrons to produce $^{\bullet}OH$.[24] Furthermore, known for its high oxidizing ability, O_3 ($E_0 = 2.07$ V_{NHE}) can pretreat easily degradable organic compounds, thereby reducing reliance on $^{\bullet}OH$ and improving the overall efficiency of reaction systems in practical applications.[25] The reduction of O_3 follows a one-electron pathway ($O_3 \rightarrow {}^{\bullet}O_3^- \rightarrow HO_3^{\bullet} \rightarrow {}^{\bullet}OH$), demonstrating a direct correlation between the yield of available electrons and $^{\bullet}OH$, making photocatalytic ozonation a powerful approach to elucidate structure–activity relationships and serving as an exemplary advanced oxidation process to alleviate environmental pollution.[26,27]

We first used density functional theory (DFT) calculations to design a highly efficient CN-based SAP. To validate the design and investigate how the integration of asymmetric triazole *versus* symmetric triazine units in the carbon nitride supports influences optoelectronic properties and photocatalytic performance, two CNs with distinct structures were synthesized: symmetric triazine-based C_3N_4 and asymmetric triazole-based C_3N_5, along with their SAPs containing iron with FeN_4 sites. Experimental characterization and theoretical calculations revealed that the anchoring of iron SAs altered the charge distribution in the CN supports and modulated the dipole field, which in turn impacted charge transfer, charge separation and reactant adsorption. Additionally, the iron SAs introduced midgap states, enhanced light absorption and modified charge decay behaviors. This study shows that the role of SAs in photocatalytic reactions is intricately linked to the structure of the support and proposes fundamental guidelines for designing active photocatalysts.

Results and discussion

CN-based SAP design *via* DFT calculation

In general, efficient photocatalysts should exhibit the following characteristics: (1) broad light-harvesting corresponding to a narrow band gap, (2) effective charge carrier separation, which can be facilitated by an internal field, and (3) abundant active sites for efficient catalytic reactivity.[9,28,29] In SAPs, the supports serve as light-harvesting units, while the SAs act as active sites. However, metal SA–support interaction significantly affects the three key reaction steps by regulating the electronic properties of the SAPs.[12] To investigate how the structural differences between symmetric triazine- and asymmetric triazole-based supports affect photocatalytic performance, we calculated the band structures and dipole moments of the SAPs and their supports to assess their light-harvesting capabilities and charge separation efficiencies, respectively, and thereby predict their theoretical photocatalytic activity. For this purpose, two commonly used CN supports, C_3N_4 and C_3N_5, and Fe as the SA were selected, due to the high photocatalytic ozonation activity of C_3N_4-based SAPs for $^{\bullet}OH$ formation reported in our previous work[30] (DFT calculation is detailed in the ESI†).

The structure of C_3N_4, C_3N_5, Fe-C_3N_4, and Fe-C_3N_5 was theoretically modeled as shown in Fig. S1.† DFT calculations reveal that C_3N_4 and C_3N_5 exhibit band gaps of 2.6 and 2.4 eV at the Γ point, respectively (Fig. 1a and b). The conduction band (CB) of both C_3N_4 and C_3N_5 primarily consists of N 2p orbitals, while the hybridization of N 2p and C 2p orbitals contributes to the formation of the valence band (VB) (Fig. S2†). When Fe is loaded in C_3N_4 and C_3N_5, the hybridization of the N 2p and Fe 3d orbitals results in an increased density of states mainly near the conduction band minimum (CBM) and valence band maximum (VBM), respectively (Fig. 1c, e, d and f). Additionally,

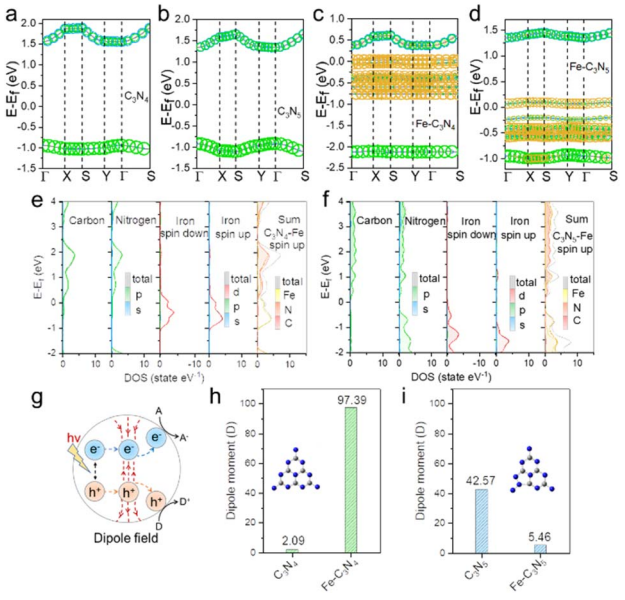

Fig. 1 The calculated electron energy bands of (a) C_3N_4; (b) C_3N_5; (c) Fe-C_3N_4; and (d) Fe-C_3N_5 (elements are represented by different colors: carbon is blue, nitrogen is green, and iron is orange, and the size of each circle represents the contribution magnitude of this element to the band). Total density of states (TDOS) of (e) Fe-C_3N_4 and (f) Fe-C_3N_5. (g) Mechanism about the accelerated separation of photocatalytic carriers induced by the dipole field effect; dipole moments (per unit cell) of (h) Fe-C_3N_4 and (i) Fe-C_3N_5, calculated based on Berry phase expressions.

the addition of iron SAs also generates intermediate states in the band gap of both C_3N_4 and C_3N_5, which enhances light absorption, increasing the production of photo-generated charges.

Additionally, the charge-transfer dynamics during photocatalytic reactions are also closely related to the interaction between iron SA and the light-harvesting support. The internal field is regarded as the common driving force for charge separation; therefore, DFT was used to estimate the dipole moment (Fig. 1g) of C_3N_4, Fe-C_3N_4, C_3N_5, and Fe-C_3N_5.[31] The dipole moment of triazine-based C_3N_4 (with a crystallographic plane group of *Pm*) was 2.09 D (Fig. 1h). Upon introducing iron SAs to form Fe-C_3N_4, the symmetry of C_3N_4 was broken, resulting in a substantial increase in the dipole moment to 97.39 D according to Fig. 1h, indicating better charge separation efficiency. In contrast, C_3N_5, composed of both triazole and triazine units, inherently exhibited a much higher dipole moment of 42.57 D than that of C_3N_4, due to its local structural asymmetry (Fig. 1i). When iron SAs were anchored onto C_3N_5 to form Fe-C_3N_5, however, the crystallographic plane group remained unchanged, but the dipole moment sharply decreased to 5.46 D. This reduction was probably due to electron redistribution caused by the introduction of Fe atoms, which have a lower electronegativity than C, thereby partially offsetting the charge distribution differences between the triazole and triazine units.[32] These results demonstrate that the effect of iron atoms on bulk charge carrier dynamics strongly depends on whether the CN support features symmetric triazine or asymmetric triazole units. It indicated that Fe-C_3N_4 would be the best photocatalyst; hence, C_3N_4, C_3N_5, Fe-C_3N_4, and Fe-C_3N_5 were further synthesized to verify this hypothesis.

Synthesis and characterization of CN-based SAPs

To load iron SAs on different CN matrices, dicyandiamide for synthesizing C_3N_4 or 3-amino-1,2,4-triazole for C_3N_5 (Fig. S3†),[16,19] was mixed with $FeCl_3 \cdot 6H_2O$. The atomically dispersed Fe was anchored on C_3N_4 (labeled Fe-C_3N_4) and C_3N_5 (Fe-C_3N_5) by a simple thermal polymerization strategy (see the Experimental section in the ESI†). Control samples of pristine C_3N_4 and C_3N_5 were also prepared for use as references. The Fe contents in Fe-C_3N_4 and Fe-C_3N_5 were 3.7 wt% and 3.8 wt%, respectively, determined by inductively coupled plasma triple quadrupole mass spectrometry (ICP-MS). Element analysis confirmed that the atomic ratios of C/N in C_3N_5 and Fe-C_3N_5 were around 0.60, whereas those in C_3N_4 and Fe-C_3N_4 were 0.67 (Table S1†), which are consistent with the literature.[17,19] Fig. 2a shows the X-ray diffraction (XRD) patterns of C_3N_5, which exhibit characteristic diffraction peaks at 13.5° and 26.9°, corresponding to the (100) and (002) planes of nitrogen-rich triazole-based CN. These peaks indicate ordered in-plane structural and interlayer stacking of aromatic systems in graphitic materials.[27,30] In comparison, C_3N_4 exhibits peaks at 13.1° and 27.4°, indicating a slightly smaller in-plane distance between each structural unit and a larger interlayer spacing in C_3N_5. The intensity of both peaks decreases greatly when iron is incorporated, presumably due to a decrease in structural

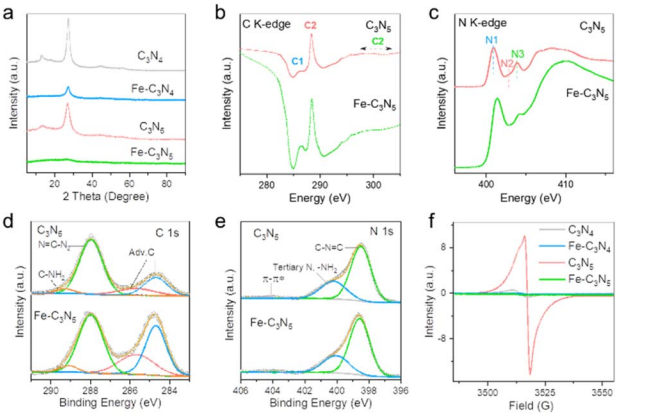

Fig. 2 Structural characterization of catalysts. (a) XRD patterns of C_3N_4, C_3N_5, Fe-C_3N_4, and Fe-C_3N_5. (b) C K-edge NEXAFS of C_3N_5 and Fe-C_3N_5. (c) N K-edge X-ray NEXAFS of C_3N_5 and Fe-C_3N_5. (d) C 1s XPS spectra of C_3N_5 and Fe-C_3N_5. (e) N 1s XPS spectra of C_3N_5 and Fe-C_3N_5. (f) EPR spectra of C_3N_4, C_3N_5, Fe-C_3N_4, and Fe-C_3N_5.

orderliness of both the stacked layer and the in-planar structure of CN supports. Significantly, no iron species-related diffraction peaks are observed in both Fe-C_3N_5 and Fe-C_3N_4, indicating the homogeneous dispersion of iron species within the CN supports.

Fourier transform infrared spectroscopy (FT-IR) analysis reveals characteristic peaks at 740–775 cm^{-1}, 810–891 cm^{-1}, 1200–1700 cm^{-1}, 2180 cm^{-1}, and 3200–3400 cm^{-1} (shown in Fig. S4†), which correspond to the heterocyclic N–N bond in the triazole group, the condensed C–N heterocycles in the triazine group, stretching modes of C–N heterocycles in triazine, cyano groups (–C≡N) formed from the terminal –C–NH_2 in the melon structural unit, and the terminal amino group of the CN framework, respectively.[17,18] These spectra confirm that both C_3N_5 and Fe-C_3N_5 comprised triazole units and triazine groups. Similarly, the FTIR analysis of C_3N_4 and Fe-C_3N_4 also corroborated the integral melon skeleton of the carbon nitride structure. Interestingly, a new peak at 2158 cm^{-1} appeared in both Fe-C_3N_4 and Fe-C_3N_5, attributed to cyano groups (–C≡N) derived from the conversion of terminal –C–NH_2 in the melon unit.[33] This change is probably induced by the presence of iron species that affected the polymerization process.[34] Calculations from the nitrogen sorption measurements (Fig. S5†) show that C_3N_5 (0.9 $m^2\ g^{-1}$) has a significantly lower specific surface area than C_3N_4 (7.1 $m^2\ g^{-1}$), whereas Fe-C_3N_5 has a higher surface area (3.8 $m^2\ g^{-1}$) than Fe-C_3N_4 (1.8 $m^2\ g^{-1}$), implying that Fe-C_3N_5 could possess more active sites for surface reactions than Fe-C_3N_4.

Synchrotron-based near-edge X-ray absorption fine structure (NEXAFS) was employed to investigate the bonding structures of C_3N_5 and Fe-C_3N_5, compared with the structures of C_3N_4 and Fe-C_3N_4. The C K-edge NEXAFS of both C_3N_5 and Fe-C_3N_5 exhibits three typical peaks of triazole-based CN (Fig. 2b): C=C (C1) at 288.1 eV, C–N–C (C2) at 289.0 eV, and C–C (C3) at 295–300 eV.[17,35] These peaks slightly shift towards higher energies for C_3N_4 and Fe-C_3N_4 (Fig. S6a†), and the weaker corresponding bonds in C_3N_5 and Fe-C_3N_5 indicate that the binding affinity

between electrons in the 1s orbital and C decreases due to the formation of a triazole moiety within the tri-*s*-triazine unit of C_3N_5. The N K-edge NEXAFS further reveals three main resonances in both CN supports and SAPs (Fig. 2c and S6b†): C–N–C (N1), graphitic three-fold nitrogen atom N-3C (N2), and sp^3 N-3C (N3) bridging among the three structural units.[17,35] These results suggest that the structure of C_3N_5 closely resembles the heptazine-based structure of C_3N_4, but with subtle variations attributed to the integration of triazole units.

X-ray photoelectron spectroscopy (XPS) was utilized to further analyze the chemical states of the samples. The survey spectra confirm that C_3N_4 and C_3N_5 are primarily composed of C and N, with a minor peak of iron observed in Fe-C_3N_4 and Fe-C_3N_5 (Fig. S7†). In the C 1s XPS spectra of C_3N_5 and Fe-C_3N_5, peaks corresponding to N_2–C=N– (288 eV), adventitious C (285.7 and 284.8 eV) and the sp^2-hybridized C in the aromatic ring attached to the NH_2 group (289.1 eV) are identified in Fig. 2d.[18,36] The peaks at 289.1 eV specifically suggest the incorporation of triazole moieties within the CN framework of C_3N_5 and Fe-C_3N_5.[17] The peak at 288 eV in C_3N_4 (288.3 eV) slightly shifted to higher energy (Fig. S8a†), which is consistent with the NEXAFS results. In the N 1 s XPS spectra of C_3N_5 and Fe-C_3N_5 (Fig. 2e), the peak at 398.5 eV is assigned to the C–N=C bond, while the peak at 400.2 eV is attributed to a combination of signals from bridging N (*e.g.*, tertiary N) and amino groups (–NH_x), indicating that C_3N_5 and Fe-C_3N_5 have a similar tri-*s*-triazine framework to C_3N_4 (Fig. S8b†).[17,37] Furthermore, signals at 403.8 eV in the N 1s XPS spectra indicate the delocalization of p electrons in CN heterocycles, likely due to the graphitic stacking of CN layers in both C_3N_5 and Fe-C_3N_5.[17]

The presence of unpaired electrons in the structural framework was investigated using electron paramagnetic resonance (EPR) spectroscopy.[36] As shown in Fig. 2f, C_3N_5 exhibited a more intense Lorentzian line compared to C_3N_4, indicating enhanced electron transport due to the presence of the triazole ring in the CN unit cell.[17] Interestingly, the introduction of iron SAs into both C_3N_4 and C_3N_5 significantly reduces this EPR signal intensity, with Fe-C_3N_4 and Fe-C_3N_5 showing comparable diminished intensity. This reduction was attributed to the unpaired electrons likely transferring from the aromatic rings of carbon atoms to the iron atoms.

The TEM image of Fe-C_3N_5 (Fig. 3a) revealed a typical lamellar structure with minor occurrences of microcracks and pores, similar to the morphology observed on Fe-C_3N_4 (Fig. 3c). No metal nanoparticles were detected on Fe-C_3N_5 or Fe-C_3N_4 in the high-resolution TEM images (Fig. S10†). The atomic-level distribution of Fe species was analyzed by using aberration-corrected high-angle annular dark field scanning transmission electron microscopy (AC-HAADF-STEM). In Fig. 3b and d, bright spots (marked by red circles) corresponding to Fe single atoms are observed across the matrices of both C_3N_4 and C_3N_5. Moreover, the energy-dispersive spectroscopy (EDS) mapping images demonstrated that both C, N, and Fe species are uniformly distributed on Fe-C_3N_4 and Fe-C_3N_5, further verifying that Fe was predominantly present as SAs rather than forming nanoparticles (Fig. S11 and S12†). This corroborates the XRD

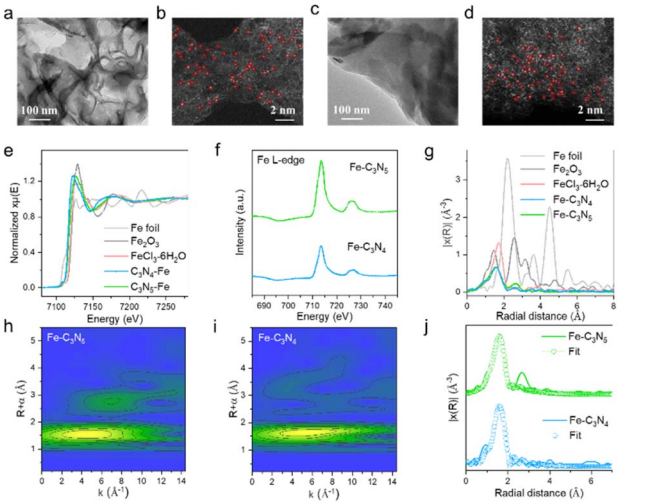

Fig. 3 Characterization of catalysts. TEM images of (a) Fe-C_3N_5 and (c) Fe-C_3N_4. Magnified HAADF-STEM images of (b) Fe-C_3N_5 and (d) Fe-C_3N_4. (e) Fe K-edge XANES spectra of Fe-C_3N_5, Fe-C_3N_4, Fe foil, Fe_2O_3, and $FeCl_3$. (f) The XANES spectra at the Fe L-edge of Fe-C_3N_5 and Fe-C_3N_4. (g) The FT-EXAFS spectra of the EXAFS spectra. (h) The best-fit analysis results of EXAFS for Fe-C_3N_5 and Fe-C_3N_4. The wavelet transform EXAFS analysis of (i) Fe-C_3N_5 and (j) Fe-C_3N_4.

findings, which show no detectable diffraction peaks corresponding to Fe oxide or metallic Fe.

To further identify the iron coordination environment in Fe-C_3N_4 and Fe-C_3N_5, Fe K-edge X-ray absorption near edge structure (XANES) measurement was conducted. As shown in Fig. 3e, the absorption edges of Fe-C_3N_4 and Fe-C_3N_5 are positioned between those of metallic Fe foil and Fe_2O_3, suggesting that the average oxidation state of Fe lies between 0 and +3. Despite similar near-edge structures, the absorption edge of Fe-C_3N_5 is slightly shifted to higher energies compared to Fe-C_3N_4, indicating that the oxidation state of Fe in Fe-C_3N_5 is higher. Similarly, the Fe L-edge XANES spectra results (Fig. 3f) show a peak at higher energy for Fe-C_3N_5 compared to Fe-C_3N_4. Fourier transformed (FT) EXAFS spectra of Fe-C_3N_4 and Fe-C_3N_5 display a single prominent peak at 1.6 Å with no detectable Fe–Fe interactions at 2.2 Å (Fig. 3g), implying that the Fe in Fe-C_3N_4 and Fe-C_3N_5 is atomically dispersed. The atomic dispersion of Fe was also supported by the wavelet-transform (WT) contour plot (Fig. 3h and i), revealing a single intensity maximum around 4 $Å^{-1}$ for both Fe-C_3N_4 and Fe-C_3N_5, characteristic of Fe–N coordination. EXAFS best-fit analysis (Table S2†) indicates that a single Fe atom in Fe-C_3N_4 and Fe-C_3N_5 was coordinated with four N atoms, forming an Fe-N_4 coordination structure, with Fe-N bond lengths of 2.10 and 2.07 Å, respectively (Fig. 3j and S13†). The proposed Fe-N_4 coordination models for Fe-C_3N_4 and Fe-C_3N_5 are illustrated in Fig. S1.† The characterization conducted confirms that the DFT predicted structure aligned well with experimental results.

Photocatalytic activity and ROS identification over different CN-based SAPs

The photocatalytic ozonation activity of catalysts for $^{\cdot}OH$ production was assessed using oxalic acid (OA) as the target

pollutant, which exhibits resistance to direct O_3 oxidation (k < 0.04 M^{-1} s^{-1}) but high reactivity with ˙OH, making it an ideal probe molecule for ˙OH.[30,38] As shown in Fig. S14,† no significant OA degradation occurs over all catalysts in either photocatalytic oxidation or catalytic ozonation processes. However, when visible light and ozone were applied simultaneously, obvious OA degradation was observed across all catalysts (Fig. 4a and S15†). The performance of the catalysts after 60 min reaction follows the sequence Fe-C_3N_4 > Fe-C_3N_5 > C_3N_5 > C_3N_4. In the case of pure supports, C_3N_5 demonstrated higher O_3 activation activity for OA degradation under visible light compared to C_3N_4. This suggests that, despite having similar active sites, the incorporation of symmetric triazine or asymmetric triazole units into CN-based SAPs can significantly affect their photocatalytic activity by altering charge carrier kinetics through differences in dipole moment. Notably, materials with Fe SAs outperformed their pristine supports, suggesting that incorporating iron atoms into C_3N_4 and C_3N_5 effectively promotes the activation of O_3 by photogenerated electrons to facilitate ˙OH generation. Additionally, Fe-C_3N_4 and Fe-C_3N_5 demonstrate superior photocatalytic ozonation activity in degrading other refractory pollutants, including phenolic compounds (bisphenol and diclofenac), antibiotics (sulfamethoxazole and cephalexin), and dyes (methylene blue) (Fig. 4b and c). Notably, Fe-C_3N_4 exhibits superior activity to Fe-C_3N_5 in total organic carbon (TOC) removal of all pollutants, consistent with OA degradation and ozone decomposition rates (Fig. 4d).

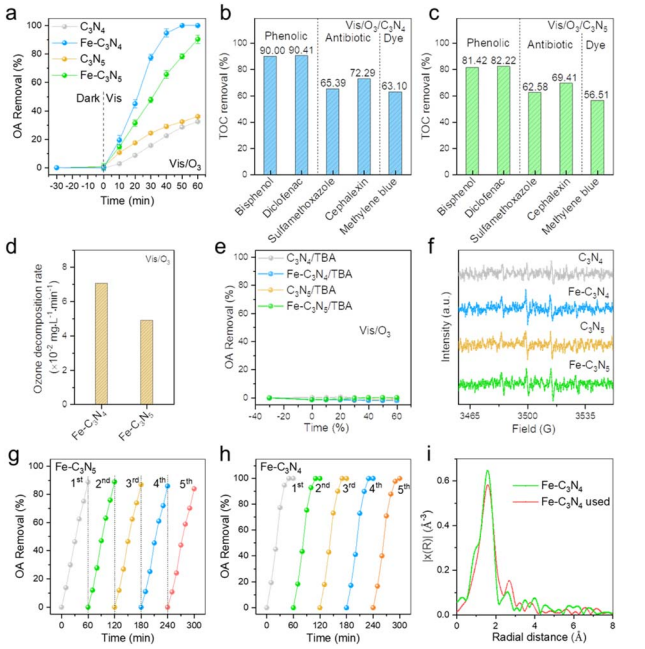

Fig. 4 (a) Degradation efficiency of OA in photocatalytic ozonation with different photocatalysts; degradation of various pollutants on (b) vis/O_3/Fe-C_3N_4 and (c) vis/O_3/Fe-C_3N_5 systems; (d) dissolved ozone decomposition rate in the photocatalytic ozonation processes. (e) Quenching using TBA in photocatalytic ozonation processes. (f) EPR spectra in the photocatalytic ozonation with DMPO as a probe. Stability of (g) Fe-C_3N_5 and (h) Fe-C_3N_4 in successive cycling (photocatalytic ozonation system). (i) Experimental Fe K-edge FT-EXAFS spectra for fresh and used Fe-C_3N_4. Conditions: [catalyst]: 0.1 g L^{-1}, [OA]: 2 mM, [O_3]: 30 mg L^{-1}, [TBA]: 100 mM, solution pH: 2.7, and solution volume: 0.3 L. Error bars represent the data from triplicate tests.

The stability of Fe-C_3N_4 and Fe-C_3N_5 in photocatalytic ozonation was assessed through recycling investigations (Fig. 4g and h), showing no noticeable decline in photocatalytic activity over five consecutive reaction cycles, indicating excellent stability. Consistently, inductively coupled plasma (ICP) analysis revealed that Fe leaching after each reaction cycle was as low as 0.03% for Fe-C_3N_4 and 0.08% for Fe-C_3N_5, further confirming the strong anchoring of Fe single atoms and the high structural stability of the catalysts. XANES spectra of the Fe K edge for used Fe-C_3N_4 after five repetitive reaction cycles exhibit a slight right-shift in the absorption edge in comparison with the fresh sample, indicating a small rise in the oxidation state of the iron species (Fig. S16†). Additionally, a negligible change in major peak positions is observed in the FT-EXAFS spectra when comparing used Fe-C_3N_4 with fresh Fe-C_3N_4 (Fig. 4i). Notably, no peaks related to an Fe–Fe bond appeared for used Fe-C_3N_4, further confirming its structural stability. Consistent with these findings, AC-HAADF-STEM images of the post-reaction Fe-C_3N_4 and Fe-C_3N_5 samples reveal that the Fe species remain atomically dispersed without any sign of aggregation or clustering (Fig. S17†). This atomic dispersion after catalysis is in good agreement with the EXAFS results and the excellent cycling stability observed in the catalytic performance tests. As summarized in Table S3,† Fe-C_3N_4 exhibits superior photocatalytic performance compared to previously reported materials for the degradation of various organic pollutants, demonstrating its clear advantage and potential in environmental applications.

Quenching experiments were performed to identify the dominant ROS in the photocatalytic ozonation system. *Tert*-butanol (TBA) was employed as a scavenger for ˙OH radicals.[39] As shown in Fig. 4e, the degradation of OA was completely inhibited when excess TBA was added, indicating the dominant role of ˙OH in OA removal over all catalysts in the photocatalytic ozonation system. EPR spectroscopy was used to characterize the formation of ˙OH radicals and 5,5-dimethyl-1-pyrroline *N*-oxide (DMPO) was used as a probe.[26,40] Fig. 4f shows the characteristic DMPO-˙OH adduct signal (a clear 1 : 2 : 2 : 1 quartet signal, g = 2.006, and $a_N = a_{H\beta}$ = 14.9 G) observed in all photocatalytic ozonation systems, with signal intensities positively correlating with the catalytic activity of the samples. These results collectively confirm that ˙OH radicals are the primary reactive species responsible for OA degradation in the photocatalytic ozonation process.

Systematic photocatalytic mechanism in the photocatalytic ozonation process

A typical photocatalytic process involves three main steps: light harvesting, charge separation and transfer, and surface catalytic reaction. For photocatalysts, improving the light absorption capacity by narrowing the band gap, introducing a driving force for charge carrier separation and transfer, and designing active sites for the target reaction are key factors for the enhancement

of photocatalytic activity. Thus, a systematic mechanistic investigation was conducted to determine how the incorporation of symmetric triazine *versus* asymmetric triazole units in CN materials influences their charge transfer dynamics and photocatalytic activity.

Light harvesting

As depicted in Fig. 5a, the UV-vis absorbance spectrum of C_3N_4 exhibits a characteristic absorption edge at 460 nm. In contrast, C_3N_5 presents an absorption edge around 540 nm, likely resulting from the p–p* electronic transitions associated with the sp^2 hybridization of C and N within the CN framework (Fig. S2†).[41] Consequently, the band gap of C_3N_5 (2.30 eV) is notably lower than that of C_3N_4 (2.70 eV) (Fig. 5b), which is consistent with the DFT calculation (Fig. 1a and b). Upon anchoring iron atoms, Fe-C_3N_4 shows stronger absorption and a light absorption onset at 650 nm attributed to electronic transitions induced by iron, but retains a peak at 460 nm similar to pristine C_3N_4. Similarly, the incorporation of iron into C_3N_5 further enhances the visible light absorption compared to C_3N_5, with the optical absorption edge shifting to approximately 785 nm. The DFT results show that the loading of iron introduces an Fe 3d peak within the band gap, leading to the emergence of mid-gap states (Fig. 1e and f). It is noteworthy that Fe-C_3N_4 and Fe-C_3N_5 exhibit stronger background absorbance at longer wavelengths beyond 880 nm compared to C_3N_4 and C_3N_5. This indicates the formation of additional sub-bandgap states induced by Fe doping. Meanwhile, the diminished EPR signal suggests a transformation of paramagnetic defects (*e.g.*, nitrogen vacancies) into EPR-silent or diamagnetic states. This apparent discrepancy implies a change in the nature or electronic configuration of the defects, rather than a straightforward increase in defect density.[26]

The VB position of the catalysts was explored based on XPS analysis and then the CB position can be determined by combining the band gap value. As shown in Fig. 5b, C_3N_5 exhibits a lower CB position and higher VB position than C_3N_4. The addition of iron narrows the band gap by shifting the VB upwards and the CB downwards in both C_3N_4 and C_3N_5. For Fe-C_3N_5, the higher levels of CB and VB than those of Fe-C_3N_4 may be due to the distinct density of states near the CBM and VBM originating from the Fe 3d orbital. For all catalysts, the reductive ability of the photo-generated electrons enables the conversion from O_3 to $^{\bullet}OH$.

Charge transfer dynamics

The charge transfer dynamics between metal SAs and CN is of essential importance for the entire photocatalytic system. A systematic investigation was conducted to explore the role of iron SAs and the effect of triazine–triazole structural motifs in CN materials on charge separation and transfer.

Steady-state and transient-state photoluminescence (PL) spectroscopy were conducted to explore the carrier migration *via* radiative recombination in the photocatalysts.[32] As shown in Fig. 5c, C_3N_5 has a lower PL intensity than C_3N_4, indicating that the radiative recombination of charges on C_3N_5 is inhibited by the dipole field.[18] Upon loading iron SAs onto the CN, the PL intensity of both Fe-C_3N_4 and Fe-C_3N_5 is lower than that of the support, indicating that Fe SAs effectively suppress radiative recombination. Time-resolved PL (TRPL) in Fig. 5d illustrates the decay kinetics of emissive states. The two components (fast decay component τ_1 and slow decay component τ_2) reflect the intraplanar recombination and interplanar or intrachain migration, respectively (Table S4†).[42,43] C_3N_5 exhibits a significantly shorter lifetime for both τ_1 and τ_2 compared to C_3N_4, which is indicative of faster charge migration in C_3N_5. This can be attributed to its larger conjugated π network due to the presence of azo bonds extending π delocalization or stronger nonradiative transitions because higher carrier mobility accelerates charge migration into trap sites, leading to increased nonradiative recombination.[44] Intriguingly, the introduction of Fe SAs results in similar decay profiles for Fe-C_3N_4 and Fe-C_3N_5 (Fig. 5d), indicating that Fe atoms have a greater effect on the decay behavior than the structure of the CN supports. For Fe-C_3N_4, both τ_1 and τ_2 decrease compared to C_3N_4, while the τ_1 and τ_2 of Fe-C_3N_5 are longer than those in C_3N_5.

To further illustrate the effects of the CN support and Fe SAs on charge decay kinetics, femtosecond transient absorption spectroscopy (fs-TAS) was performed to monitor the electron trapping process (Fig. 5f–i). The probed wavelength was 4000 nm, allowing differentiation between the shallow trapping process, band gap recombination (visible light range), and deep trapping (near-infrared range).[45] For C_3N_4 and C_3N_5, the transient absorption (TA) time profiles were fitted using two and three exponential components, respectively (Fig. 5f and h). The fast decay component (τ_1) for C_3N_4 was attributed to intra-band electron transitions, the intermediate component (τ_2) to the

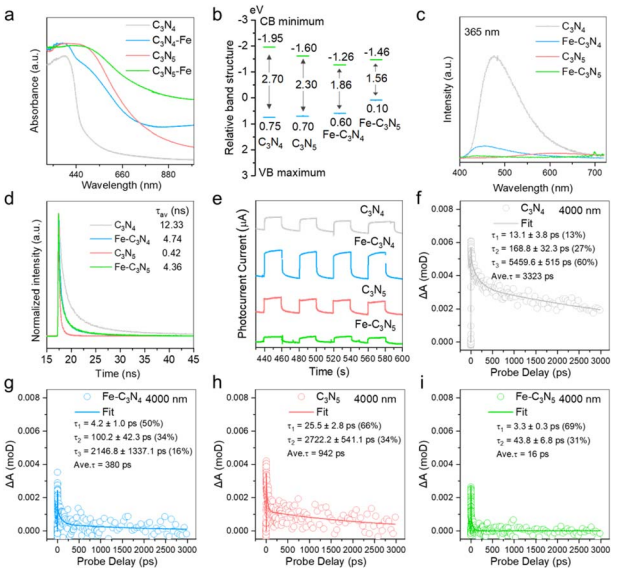

Fig. 5 (a) The diffuse reflectance spectra, (b) band diagrams, (c) steady-state PL spectra, (d) transient-state PL spectra, and (e) photoelectrochemical tests of C_3N_4, C_3N_5, Fe-C_3N_4, and Fe-C_3N_5. TA kinetic plots and representative fitting curves of (f) C_3N_4, (g) Fe-C_3N_4, (h) C_3N_5, and (i) Fe-C_3N_5.

trapping process,[46] and the slow decay component (τ_3) to recombination in trap states.[47,48] For C_3N_5, τ_1 corresponds to electron transition/trapping and τ_2 to trapped electron recombination. Notably, the percentage of the slow decay component in C_3N_5 was markedly reduced compared to C_3N_4, indicating that a greater proportion of electrons in C_3N_5 could participate in photocatalytic reactions.[49]

Upon introducing Fe SAs, the TA fitting results for Fe-C_3N_4 and Fe-C_3N_5 are given in Fig. 5i and j. In Fe-C_3N_4, all three decay components show shorter lifetimes than those in C_3N_4, with increased contributions from the fast and intermediate decay components. Similarly, Fe-C_3N_5 exhibits shorter τ_1 and τ_2 compared to C_3N_5. These results suggest that electrons are captured by the Fe SAs.[50] This aligns with the TRPL results, confirming that Fe atoms significantly alter the charge decay process. Since the slow decay component was reduced in Fe-C_3N_4 and Fe-C_3N_5 compared to their pristine supports, both SAPs exhibit superior photocatalytic performance to their supports.[9] In addition, the accelerated migration of electrons to Fe SAs suggests that Fe atoms may serve as the active sites in SAPs, facilitating interfacial electron transfer and enabling more electrons to access the surface to participate in O_3 reduction.

The distinct impact of symmetric triazine *versus* asymmetric triazole structures in CN-based SAPs on the separation of electrons and holes is further supported by the transient photocurrent responses of samples.[51] As shown in Fig. 5e, C_3N_5 exhibits a higher photocurrent density than C_3N_4, most likely arising from the dipole field caused by the asymmetric structure. Fe-C_3N_4 produces significantly higher photocurrent density than C_3N_4. In contrast, the photocurrent density of Fe-C_3N_5 is lower than that of C_3N_5. Generally, an Fe–N bond forms between tri-*s*-triazine units, accelerating the transfer of electrons.[30] Considering that the symmetrical structure of C_3N_4 is broken when iron SAs are doped, the enhanced dipole field would facilitate charge separation. Nevertheless, the addition of iron SAs decreases the dipole field on C_3N_5, which has an asymmetrical structure, and thus an opposite trend appears. It is also noted that Fe-C_3N_5 exhibits better OA degradation efficiency than C_3N_5, most likely due to the role of the iron SAs in the surface reaction (discussed later). As shown in Fig. S18,† the Nyquist circle diameters of both C_3N_4 and C_3N_5 are smaller than those of Fe-C_3N_4 and Fe-C_3N_5, respectively. Hence, the anchoring of iron SAs between light-harvesting units facilitates the conductivity and mobility of electrons.

To gain deeper insight into the reaction mechanism, the structure and frontier orbital of the catalyst were studied (Fig. 6a–d). The highest occupied molecular orbital (HOMO) and the lowest unoccupied molecular orbital (LUMO) represent the electron distribution states before and after light excitation, respectively.[52] For C_3N_4, a uniform spatial distribution of electrons on the LUMO and holes on the HOMO was observed (Fig. 6a), indicating a high tendency for electron–hole recombination. In contrast, C_3N_5 exhibited a more uneven spatial charge distribution due to the formation of a dipole field that facilitated charge separation (Fig. 6b). With the presence of iron SAs, Fe-C_3N_4 displays a stronger electron distribution

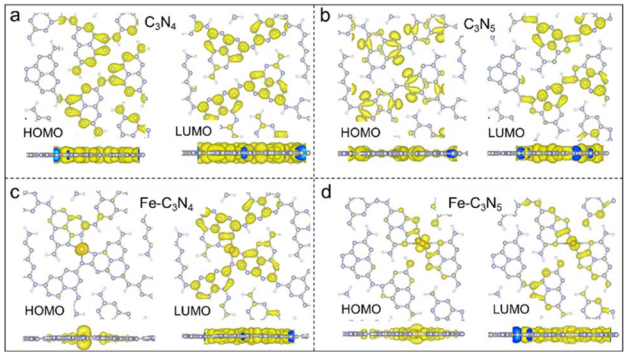

Fig. 6 Top and side perspectives of the calculated charge distribution for the HOMO and LUMO of (a) C_3N_4, (b) C_3N_5, (c) Fe-C_3N_4, and (d) Fe-C_3N_5. The yellow color highlights electron accumulation at an isosurface value of 0.001 Å e^{-3}. Each color is associated with a specific element: white represents carbon, blue stands for nitrogen, red for oxygen, and orange for iron.

asymmetry, confirming the role of iron atoms in electron accumulation and accelerated charge separation. However, Fe SAs in C_3N_5 did not lead to a more asymmetric charge distribution (Fig. 6c and d). In other words, Fe-C_3N_5 exhibits a more symmetric electron distribution than Fe-C_3N_4, indicating more severe carrier recombination and consequently lower photocatalytic ozonation activity. These findings reveal that the CN support structure influences the role of the iron SAs in charge carrier dynamics by regulating dipole moment. It is noted that charge density is concentrated around iron SAs in both Fe-C_3N_4 and Fe-C_3N_5, implying that effective interfacial charge transfer was primarily eased *via* the formation of strong Fe–N coordination bonds.

Surface catalytic reaction

In the photocatalytic ozonation process, multiple reaction pathways occur because of the high reactivity of O_3 and the coexistence of O_3 and O_2, as shown in Fig. 7a.[27,53,54] Achieving high $^{\bullet}OH$ production efficiency requires boosting the $1e^-$ ozone reduction reaction. The number of electrons transferred in the photocatalytic ozonation process was determined by rotating ring disc electrode analysis. The estimated electron transfer number (n) for all catalysts under light irradiation was close to 1 (Fig. 7b), indicating a dominant light-driven $1e^-$ reduction pathway.

To further understand this behavior, DFT calculation was conducted to gain insight into the adsorption of O_3 on the surface of the catalysts (Fig. 7c). The Fermi level (E_f) of C_3N_5 shifts positively to −4.22 eV compared to that of C_3N_4 (−5.05 eV), probably due to the presence of the electron-rich triazole groups. When introducing iron SAs, the E_f shows a large upward shift (Fig. 7d). Since a more positive Fermi level contributes to electron migration to the catalyst surface, C_3N_5 enables more efficient interfacial electron transfer than C_3N_4, as reflected by the higher energy of O_3 adsorption (−0.27 eV for C_3N_5 and −0.16 eV for C_3N_4) (Fig. 7b). Similarly, the incorporation of iron SAs further increases the Fermi level (Fig. 7d) and provides

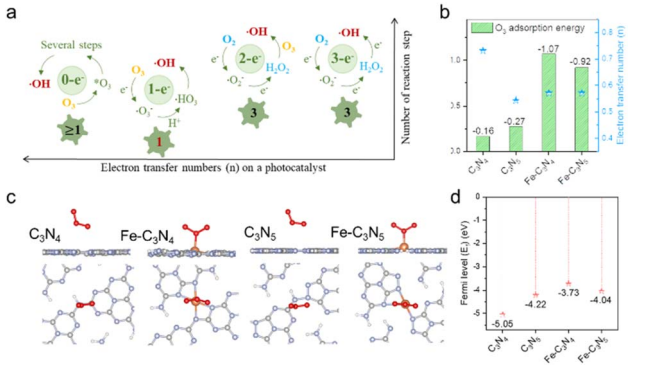

Fig. 7 A schematic diagram illustrating the intermediates involved in the multielectron-transfer processes in photocatalytic ozonation. (a) The most efficient reaction for OH generation is the one-electron-reduction reaction; (b) the O_3 adsorption energy and electron transfer number of C_3N_4, C_3N_5, Fe-C_3N_4, and Fe-C_3N_5; (c) the adsorption configuration of O_3 in C_3N_5 and Fe-C_3N_5 from top and side views; (d) the calculated Fermi levels (E_f) of C_3N_4, C_3N_5, Fe-C_3N_4, and Fe-C_3N_5.

active sites, enhancing O_3 adsorption energy on both Fe-C_3N_4 and Fe-C_3N_5. Their less negative Fermi level promotes electron transfer towards O, facilitating the formation of an Fe–O bond (Fig. 7c). As a result, the photogenerated charges reach the surface more readily, making them more accessible to be captured by O_3 to generate $^{\bullet}OH$, and thus improving the photocatalytic ozonation performance of Fe-C_3N_4 and Fe-C_3N_5.

A systematic catalytic mechanism in the photocatalytic ozonation process was proposed based on the above characterization and analysis. For the CN supports, C_3N_5 exhibits a narrower band gap, a stronger dipole field that accelerates charge carrier separation and transfer, and stronger O_3 adsorption capability than C_3N_4. Consequently, better photocatalytic ozonation performance was observed for C_3N_5 compared with C_3N_4. Upon loading iron, the separation and migration of bulk charge carriers in C_3N_4 are enhanced, while those are weakened in C_3N_5 due to the distinct manipulation of the dipole moment. Additionally, photo-generated electrons are concentrated around iron SAs in both Fe-C_3N_4 and Fe-C_3N_5, and effective interfacial charge transfer occurs *via* the formation of strong Fe–N coordination bonds, leading to stronger interaction with O_3 and accelerated photocatalytic reactions. Therefore, despite more charge carrier recombination and a similar E_f in Fe-C_3N_5 compared to C_3N_5, the enhanced interfacial electron transfer contributed to superior O_3 adsorption and photocatalytic activity of Fe-C_3N_5. Meanwhile, Fe-C_3N_4, featuring both uneven charge distribution and efficient interfacial electron transfer, achieved the highest photocatalytic performance in ozonation.

Conclusions

The impact of the structural properties of a polymer-based support on the role of SAs was explored based on DFT predictions and experimental verification. Band structures and dipoles were calculated as key factors to identify high photoactivity, and the experiment verified excellent performance of the optimal sample determined by DFT calculation. Combining in-depth structural and optoelectronic characterization, the results revealed that the iron SAs play a distinct role in charge separation and transfer on different supports. The addition of iron SAs weakens the dipole field in C_3N_5 but strengthens it in C_3N_4. Consequently, the addition of iron SAs onto C_3N_4 leads to more even spatial distribution of electrons to accelerate the separation of photo-generated charge carriers, while on C_3N_5 it decreases the recombination of electrons and holes. This work underscores the impact of the structure of the light-harvesting unit on regulating the role of SAs in the photocatalytic mechanism and proposes foundational guidelines for designing active photocatalysts.

Data availability

The data supporting this article have been included as part of the ESI.†

Author contributions

H. C. and Y. X. supervised the research. J. W. Y. X. and H. C. conceived the ideas and designed the experiments. J. W., J. Q., Y. X., Z. W., S. L. and Y. W. performed the experiments, electrochemical measurements, materials characterization and data analysis. H. M. and R. C. performed the DFT calculation. J. W., H. M., R. C. and Y. X. wrote the manuscript. All authors discussed the experiments and commented on the manuscript.

Conflicts of interest

There are no conflicts to declare.

Acknowledgements

This work was financially supported by the National Natural Science Foundation of China (52470096 and 22478426) and the strategic priority research program of the Chinese Academy of Sciences (XDA0430105). It was carried out with the support of the 4B9A beamline at the Beijing Synchrotron Radiation Facility. This work was also supported by the Australian Research Council (ARC) Discovery Early Career Researcher Award (DE250100886) and computational resources provided by the Australian National Computational Infrastructure (NCI) under the National Computational Merit Allocation Scheme 2025 (NCMAS 2025).

References

1 D. Nguyen and T. Do, *Adv. Mater. Interfaces*, 2023, **10**, 2201413.
2 P. Chen, M. Zhou, Y. Liu, B. Li, C. Chen, X. Duan and Y. Wang, *Appl. Catal., B*, 2024, **346**, 123767.
3 H. Su, H. Yin, R. Wang, Y. Wang, W. Orbell, Y. Peng and J. Li, *Appl. Catal., B*, 2024, **348**, 123683.
4 P. Zhou, M. Luo and S. Guo, *Nat. Rev.*, 2022, **6**, 823–838.

5 A. Wang, J. Li and T. Zhang, *Nat. Rev.*, 2018, **2**, 65–81.
6 S. Mitchell and J. Pérez-Ramírez, *Nat. Commun.*, 2020, **11**, 4302.
7 Y. Guo, M. Wang, Q. Zhu, D. Xiao and D. Ma, *Nat. Catal.*, 2022, **5**, 766–776.
8 M. Gawande, P. Fornasiero and R. R. Zbořil, *ACS Catal.*, 2020, **10**, 2231–2259.
9 C. Gao, J. Low, R. Long, T. Kong, J. Zhu and Y. Xiong, *Chem. Rev.*, 2020, **120**(21), 12175–12216.
10 A. Moutsiou, A. Olivati, L. Cipriano, A. Sivo, S. Collins, Q. Ramasse, I. Kwon, G. Liberto, M. Kanso, R. Wojcieszak, G. Pacchioni, A. Petrozza and G. Vilé, *ACS Catal.*, 2025, **15**, 5601–5613.
11 B. Singh, M. Gawande, A. Kute, R. Varma, P. Fornasiero, P. McNeice, R. Jagadeesh, M. Beller and R. Zbořil, *Chem. Rev.*, 2021, **121**, 13620–13697.
12 J. Ran, A. Talebian-Kiakalaieh and S. Qiao, *Adv. Energy Mater.*, 2024, 2400650.
13 W. Ong, L. Tan, Y. Ng, S. Yong and S. Chai, *Chem. Rev.*, 2016, **116**, 7159–7329.
14 Y. Akinaga, T. Kawawaki, H. Kameko, Y. Yamazaki, K. Yamazaki, Y. Nakayasu, K. Kato, Y. Tanaka, A. Hanindriyo, M. Takagi, T. Shimazaki, M. Tachikawa, A. Yamakata and Y. Negishi, *Adv. Funct. Mater.*, 2023, **33**, 2303321.
15 Q. Luo, Y. Li, X. Huo, L. Li, Y. Song, S. Chen, H. Lin and N. Wang, *Adv. Sci.*, 2022, **9**, 2105346.
16 Z. Chen, S. Mitchell, E. Vorobyeva, R. Leary, R. Hauert, T. Furnival, Q. Ramass, J. Thomas, P. Midgley, D. Dontsova, M. Antonietti, S. Pogodian, N. Lopez and J. Perez-Ramirez, *Adv. Funct. Mater.*, 2017, **27**, 1605785.
17 G. Mane, S. Talapaneni, K. Lakhi, H. Ilbeygi, U. Ravon, K. Al-Bahily, T. Mori, D. Park and A. Vinu, *Angew. Chem., Int. Ed.*, 2017, **56**, 8481–8485.
18 Z. Li, Y. Zhou, Y. Zhou, K. Wang, Y. Yun, S. Chen, W. Jiao, L. Chen, B. Zou and M. Zhu, *Nat. Commun.*, 2023, **14**, 5742.
19 J. Zhang, B. Jing, Z. Tang, Z. Ao, D. Xia, M. Zhu and S. Wang, *Appl. Catal., B*, 2021, **289**, 120023.
20 C. Martine-Huitle and L. Andrade, *Quim. Nova*, 2011, **34**, 850–858.
21 Y. Tan, W. Chen, G. Liao, X. Li, J. Wang, Y. Tang and L. Li, *Appl. Catal., B*, 2022, **306**, 121133.
22 M. Li, P. Wang, Z. Ji, Z. Zhou, Y. Xia, Y. Li and S. Zhan, *Appl. Catal., B*, 2021, **289**, 120020.
23 J. Lin, W. Tian, Z. Guan, H. Zhang, X. Duan, H. Wang, H. Sun, Y. Fang, Y. Huang and S. Wang, *Adv. Funct. Mater.*, 2022, **32**, 2201743.
24 J. Xiao, Y. Xie, J. Rabeah, A. Bruckner and H. Cao, *Acc. Chem. Res.*, 2020, **53**, 1024–1033.
25 G. Yu, Y. Wang, H. Cao, H. Zhao and Y. Xie, *Environ. Sci. Technol.*, 2020, **54**, 5931–5946.
26 J. Xiao, Q. Han, H. Cao, J. Rabeah, J. Yang, Z. Guo, L. Zhou, Y. Xie and A. Bruckner, *ACS Catal.*, 2019, **9**, 8852–8861.
27 J. Wang, G. Yu, Y. Wang, S. Liu, J. Qiu, Y. Xu, Z. Wang, Y. Wang, Y. Xie and H. Cao, *Adv. Funct. Mater.*, 2023, **33**, 2215245.
28 X. Li, H. Mai, J. Lu, X. Wen, T. Le, S. Russo, D. Winkler, D. Chen and R. Caruso, *Angew. Chem., Int. Ed.*, 2023, **62**, e202315002.
29 H. Mai, D. Chen, Y. Tachibana, H. Suzuki, R. Abe and R. Caruso, *Chem. Soc. Rev.*, 2021, **50**, 13692–13729.
30 J. Wang, J. Qiu, Z. Wang, Z. Zhuang, S. Liu, Y. Wang, Y. Weng, D. Wang, Y. Xie and H. Cao, *J. Catal.*, 2024, **439**, 115772.
31 Z. Liu, C. Zhang, L. Liu, T. Zhang, J. Wang, R. Wang, T. Du, C. Yang, L. Zhang, L. Xie, W. Zhu, T. Yue and J. Wang, *Adv. Mater.*, 2021, **33**, 2104099.
32 T. Wang, C. Hsiao, S. Chen, Y. Cheng and L. Chen, *Polyhedron*, 2015, **102**, 216–223.
33 Y. Zhao, P. Zhang, Z. Yang, L. Li, J. Gao, S. Chen, T. Xie, C. Diao, S. Xi, B. Xiao, C. Hu and C. Choi, *Nat. Commun.*, 2021, **12**, 3701.
34 Y. Li, Z. Wang, T. Xia, H. Ju, K. Zhang, R. Long, Q. Xu, C. Wang, L. Song, J. Zhu, J. Jiang and Y. Xiong, *Adv. Mater.*, 2016, **28**, 6959–6965.
35 I. Kim, S. Kim, X. Jin, S. Premkumar, G. Chandra, N. Lee, G. Mane, S. Hwang, S. Umapathy and A. Vinu, *Angew. Chem., Int. Ed.*, 2018, **57**, 17135–17140.
36 Q. Han, B. Wang, J. Gao and L. Qu, *Angew. Chem., Int. Ed.*, 2016, **55**, 10849–10853.
37 C. Wu, G. Yu, Y. Yin, Y. Wang, L. Chen, Q. Han, J. Tang and B. Wang, *Small*, 2020, **16**, 2003162.
38 P. Faria, J. Orfao and M. Pereira, *Appl. Catal., B*, 2008, **79**, 237–243.
39 Z. Zhang, P. Duan, J. Zheng, Y. Xie, C. Bai, Y. Sun, X. Chen, F. Chen and H. Yu, *Nat. Commun.*, 2025, **16**, 115.
40 X. Zhu, Y. Wang, X. Duan, P. Wang, S. Zhong, S. Ren, X. Xu, B. Gao, J. Vongsvivut and S. Wang, *Adv. Mater.*, 2024, **36**, 2401454.
41 C. Wu, G. Yu, Y. Yin, Y. Wang, L. Chen, Q. Han, J. Tang and B. Wang, *Small*, 2020, **16**, 2003162.
42 B. Choudhury, K. Pual, D. Sanyal, A. Hazarika and P. Giri, *J. Phys. Chem. C*, 2018, **122**, 9209–9219.
43 S. Cao, H. Li, T. Tong, H. Chen, A. Yu, J. Yu and H. Chen, *Adv. Funct. Mater.*, 2018, **28**, 1802169.
44 P. Kumar, E. Vahidzadeh, U. Thakur, P. Kar, K. Alam, A. Goswami, N. Mahdi, K. Cui, G. Bernard, V. Michaelis and K. Shankar, *J. Am. Chem. Soc.*, 2019, **141**, 5415–5436.
45 R. Kuriki, H. Matsunaga, T. Nakashima, K. Wada, A. Yamakata, O. Ishitani and K. Maeda, *J. Am. Chem. Soc.*, 2016, **138**, 5159–5170.
46 A. Yamakata, T. Ishibashi and H. Onishi, *Phys. Lett.*, 2001, **333**, 271–277.
47 A. EI-Zohry, B. Turedi, A. Alsalloum, P. Maity, O. Bakr, B. Ooi and O. Mohammed, *Commun. Chem.*, 2022, **5**, 67.
48 V. Nikolaou, C. Govind, E. Balanikas, J. Bharti, S. Diring, E. Vauthey, M. Robert and F. Odobel, *Angew. Chem., Int. Ed.*, 2024, **63**, e202318299.
49 R. Godin, Y. Wang, M. Zwijnenburg, J. Tang and J. Durrant, *J. Am. Chem. Soc.*, 2017, **139**, 5216–5224.
50 L. Lin, Y. Ma, J. Vequizo, M. Nakabayashi, C. Gu, X. Tao, H. Yoshida, Y. Pihosh, Y. Nishina, A. Yamakata,

N. Shibata, T. Hisatomi, T. Takata and K. Domen, *Nat. Commun.*, 2024, **15**, 397.
51 Z. Zhang, L. Ren, H. Li, D. Jiang, Y. Fang, H. Du, G. Xu, C. Zhu, H. Li, Z. Lu and Y. Yuan, *Small*, 2023, **19**, 2207173.
52 S. Gumber, S. Agrawal and O. Prezhdo, *J. Phys. Chem. Lett.*, 2022, **13**, 1033–1041.
53 Y. Tan, W. Chen, G. Liao, X. Li, J. Wang, J. Wang, Y. Tang and L. Li, *Appl. Catal., B*, 2024, **351**, 124005.
54 H. Cao, J. Wang, J. Kim, Z. Guo, J. Xiao, J. Yang, J. Chang, Y. Shi and Y. Xie, *Appl. Catal., B*, 2021, **296**, 120362.